Faraday Discussions

Cite this: DOI: 10.1039/d1fd00052g

ROYAL SOCIETY OF CHEMISTRY

PAPER

View Article Online
View Journal

Electrochemically probing exciton transport in monolayers of two-dimensional semiconductors†

Chloe L. Tolbert and Caleb M. Hill *

Received 13th August 2021, Accepted 29th September 2021
DOI: 10.1039/d1fd00052g

Two-dimensional semiconductors (2DSCs) are attractive for a variety of optoelectronic and catalytic applications due to their ability to be fabricated as wide-area, monolayer-thick films and their unique optical and electronic properties which emerge at this scale. One important class of 2DSCs are the transition metal dichalcogenides (TMDs), which are of particular interest as absorbing layers in ultrathin optoelectronic devices. While TMDs are known to exhibit excellent photovoltaic properties at the bulk level, it is not yet clear how carriers are transported in these materials at thicknesses approaching the monolayer limit, where distinct changes in band structure and the nature of photogenerated carriers occur. Here, it is demonstrated that electrochemical microscopy techniques can be employed as powerful tools for visualizing these processes in 2DSCs, even within individual monolayers. Carrier generation-tip collection scanning electrochemical cell microscopy (CG-TC SECCM), which utilizes spatially-offset optical and pipet-based electrochemical probes to locally generate and detect photogenerated carriers, was applied to visualize carrier generation and transport within well-defined n-WSe_2 samples prepared *via* mechanical exfoliation. Data from these experiments directly reveal how carrier transport varies within complex 2DSC structures as layer thicknesses approach the monolayer limit. These results not only provide valuable new insights into carrier transport within monolayer TMD materials, but also demonstrate electrochemical imaging to be a powerful, yet underutilized approach for visualizing solid-state processes in semiconducting materials.

Introduction

Two-dimensional semiconductors (2DSCs) such as the transition metal dichalcogenides (TMDs) are attractive materials for a variety of optoelectronic applications due to their ability to be prepared as atomically-thin layers and the

Department of Chemistry, University of Wyoming, 1000 E. University Ave., Laramie, WY 82071, USA. E-mail: caleb.hill@uwyo.edu

† Electronic supplementary information (ESI) available: Additional data, details on finite element simulations, and SECCM movies for figures 2, 3, and 4. See DOI: 10.1039/D1FD00052G

interesting properties they exhibit at this scale.[1,2] At monolayer thicknesses, the band structure of many 2DSCs changes significantly, adopting direct bandgaps which yield strong photoluminescence (PL)[3–5] as well as exhibiting multiple local minima, or "valleys", which could potentially be utilized for information processing.[6,7] This, along with the large absorption coefficients exhibited by these materials, make them especially attractive as absorbing layers in photovoltaic cells and other optoelectronic devices.[8–14] In order to design efficient 2DSC-based devices for these applications, it is critically important to understand how photogenerated carriers are transported within 2DSCs and how transport can be controlled in a rational manner.

At the monolayer limit, photogenerated carriers in TMDs become excitonic in nature due to strong confinement in the *xy*-plane and weak dielectric screening, resulting in strong exciton binding energies on the order of several hundred meV.[15–20] This presents unique challenges in optoelectronic applications, as excitons are neutral carriers which cannot be directly influenced by applied fields. Excitons thus move primarily *via* diffusion, so understanding this process, and how different structural motifs/defects within TMDs affect it, is of critical importance. Previous studies carried out to visualize exciton transport within TMDs have employed different optical microscopy techniques (PL or transient absorption) which leverage the favourable optical properties of monolayer samples.[21–25] While this approach has been successful in visualizing carrier transport within pristine monolayer systems, it cannot be applied in more complex structures which lack a clear optical signature for the carriers of interest.

Recently, our laboratory has been exploring how pipet-based electrochemical techniques, such as scanning electrochemical cell microscopy (SECCM),[26–37] can be employed as powerful tools for visualizing carrier transport in 2DSCs. In this approach, carrier generation-tip collection (CG-TC) SECCM, an electrolyte-filled pipet is utilized to detect photogenerated carriers as they drive reactions at a nm-scale electrochemical interface. CG-TC SECCM allows carrier transport to be directly visualized by measuring these photocurrents as a function of probe position, which was recently demonstrated in studies of bulk n-WSe_2.[38] Here, studies are described applying CG-TC SECCM to visualize carrier transport in WSe_2 structures approaching the monolayer limit, ultimately revealing surprisingly long exciton transport distances in WSe_2 monolayers.

Experimental methods

Sample preparation

Bulk n-WSe_2 crystals with dopant densities of $\sim 10^{17}$ cm^{-3} were donated by Prof. Bruce Parkinson. The crystals were mechanically exfoliated immediately before experiments using Scotch tape and transferred to clean indium tin oxide (ITO)-coated cover glass slides (22 × 22 mm, #1.5, 30–60 Ω $sq.^{-1}$, SPI) using a PDMS-assisted dry transfer approach to help preserve the integrity of the nanoflakes (Gel-Pak, Gel Film, Pf-40/17-X4). The samples were left for a minimum of 24 hours to allow for complete van der Waals adherence between the nanoflakes and the ITO. Samples were stored in enclosed plastic containers when not in use, and all data was acquired within one week of initial preparation.

Sample characterization

Atomic force microscopy (AFM) imaging was carried out using a Cypher ES AFM in tapping mode with standard probes (Nanosensors, PPP-NCHR-20, n-Si, 0.01–0.02 Ω cm). We note that AFM imaging showed no significant evidence of organic contaminants on the surface of the samples discussed in this report. PL imaging was carried out using a custom PL lifetime microscope. Samples were mounted on a 2-axis piezo stage (PI P546.2C7) on an inverted optical microscope and illuminated with a pulsed laser diode (485 nm, FWHM = 110 ps, Picoquant) through a 100×, NA = 0.9 objective. Emitted PL from the sample was collected through the same objective, filtered to remove excitation light, and directed into a non-polarizing 90 : 10 beamsplitter. One beam from the beamsplitter was directed onto the slit of a spectrometer-CCD combo (Andor SR-303i-B, Newton EMCCD) and the other was focused onto an avalanche photodiode (MPD) connected to a TCSPC system (Picoquant Picoharp 300). All PL and SECCM data were acquired under low excitation power (<35 μW) to avoid effects due to exciton–exciton annihilation (see Fig. S1 in ESI†).

Probe fabrication and characterization

SECCM probes were fabricated from quartz capillaries (1.2 mm outer diameter, 0.9 mm inner diameter, Sutter) using a Sutter P-2000 pipet puller. A two-line program was employed to yield *ca.* 500 nm diameter probes (heat = 750, fil = 4, vel = 30, delay = 150, pull = 80/heat = 685, fil = 3, vel = 30, delay = 135, pull = 150). These probes were filled with an electrolyte consisting of 0.01 M I_2 (Mallinckrodt, U.S.P Grade) and 0.10 M NaI (Sigma Aldrich, ≥ 99%). The geometry of the fabricated probes evaluated using SEM imaging (FEI Quanta FEG 450, 2 keV accelerating voltage).

CG-TC SECCM studies

A home-built setup was used to conduct all SECCM studies. ITO slides containing the WSe_2 samples were attached to a ceramic holder, mounted onto an inverted optical microscope, and illuminated locally with a 633 nm laser (ThorLabs) focused through a 40×, 0.5 NA objective. An optical chopper (Thorlabs) set at 20 Hz was used to distinguish photocurrents during the experiments depicted in Fig. 3 and 4. Probes were completed by inserting a Ag/AgI wire into the electrolyte solution, and all potentials were referenced *vs.* this electrode. Completed probes were then mounted to a 3-axis piezo system (PI NanoCube). The SECCM probes were translated towards the sample while applying a cathodic bias to the ITO substrate, and probe–sample contact was detected as a sudden spike in current. A triangular potential waveform was then applied to the sample and the resulting current was recorded before retracting the probe and repeating this process at another location on the sample. Electrochemical measurements were made using a patch-clamp style amplifier (Dagan CHEM-CLAMP) and all instrumentation was controlled through custom LabView software.

Results and discussion

Carrier generation-tip collection SECCM

The basic principle of CG-TC SECCM is illustrated in Fig. 1. A semiconducting sample is immobilized on a conducting substrate and illuminated locally with

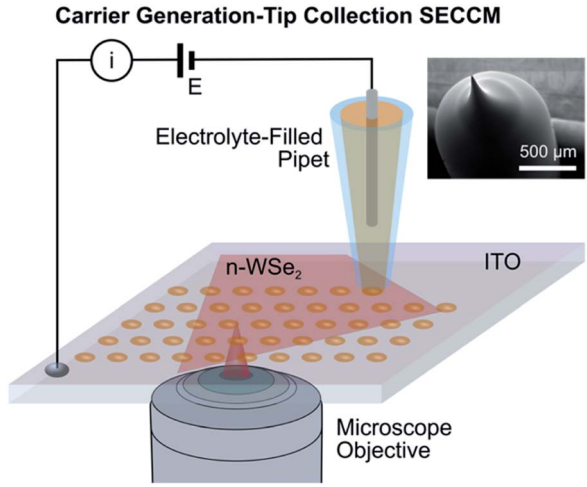

Fig. 1 Carrier generation-tip collection scanning electrochemical cell microscopy. An electrolyte-filled pipet is brought into contact with a semiconducting sample, establishing a local photoelectrochemical interface in the vicinity of a focused excitation source. By examining the resulting photocurrents as a function of probe location, carrier transport within a material can be directly visualized. The inset shows an SEM image taken of a representative SECCM probe.

a focused laser beam. If the energy of incident photons is greater than the bandgap of the semiconducting material, the excitation of electrons from the valence band to the conduction band will create mobile carriers. These photogenerated carriers will then begin to move outward from the excitation source *via* diffusion and migration (field driven transport). In CG-TC SECCM, the presence of carriers is interrogated using an SECCM probe to define a photoelectrochemical interface at a defined distance from the excitation source. Photogenerated carriers which reach this interface can drive electrochemical reactions, giving rise to a measurable current. By carrying out voltammetric measurements with the probe positioned across an array of points spanning the excitation source, carrier transport within the material can be directly visualized through electrochemical "movies" which show how photocurrents vary as a function of spatial position and applied potential. More details on the fundamentals of this technique can be found in a recent publication from our lab.[38]

Transport within bulk WSe_2

CG-TC SECCM was first applied to probe carrier transport within exfoliated layers of n-type WSe_2 (n-WSe_2) with thicknesses greater than 10 nm. At these thicknesses, 2DSCs such as WSe_2 behave electronically as "bulk" materials. Probe–sample contact thus generates a space-charge layer in the 2DSC which extends outwardly from the solid–electrolyte interface. For an n-type semiconductor under depletion conditions, the thickness of this layer can be estimated using the following equation:

$$d_{sc} = \sqrt{\frac{\varepsilon\varepsilon_0\left(E - E_{fb}\right)}{2qn_D}}$$

Here, ε is the dielectric constant of the material, ε_0 is the vacuum permittivity, E is the applied potential, E_{fb} is the flatband potential, q is the elementary unit of charge, and n_D is the dopant concentration in the semiconductor (*ca.* 10^{17} cm^3). Taking ε to have in-plane and out-of-plane values of 16 and 8,[39,40] respectively, the corresponding space charge layer thicknesses are ~110 nm and 80 nm. In the experiments presented here, the WSe_2 layers are well below this thickness, resulting in roughly linear potential profiles along the *z*-axis. These fields are highly confined, however, to within a few hundred nm from the pipet in the *xy*-plane. Given the μm-scale distances involved in these studies, the exact shape of this space charge region has a negligible impact on these experiments.

Example data from CG-TC SECCM studies of a 25 nm thick, defect-free n-WSe_2 layer is given in Fig. 2. While the layer itself exhibited lateral dimensions on the order of several hundred μm, measurements were obtained within a small, 30 μm × 30 μm square region free from any visible defects. The probe reaction employed was iodide oxidation/reduction:

$$3I^- + 2h^+ \rightleftharpoons I_3^-$$

Free carriers created within the excitation region diffused outward within the n-WSe_2 sheet. Carriers reaching the space charge region surrounding the pipet are separated by the large fields present and holes are driven to the electrochemical interface. At the interface, these holes oxidize I^- to I_2/I_3^-, resulting in a measurable photocurrent.

Photocurrent maps obtained in the vicinity of the excitation are provided in Fig. 2b. At cathodic potentials (0.45 V), photocurrents are highly localized,

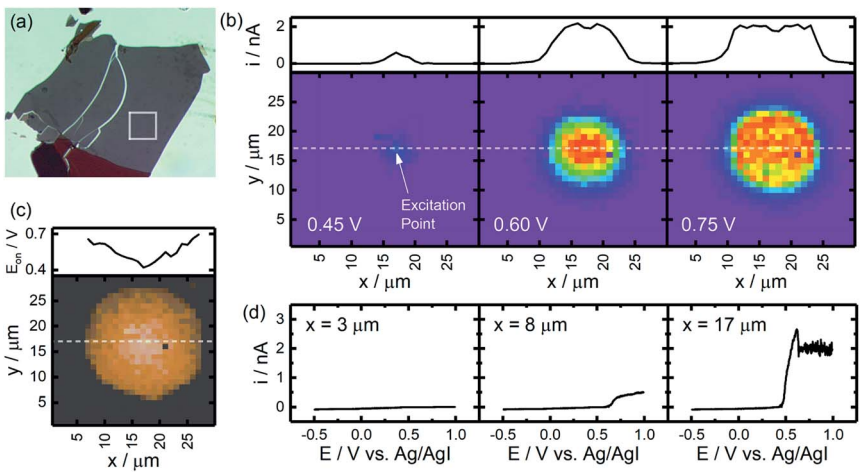

Fig. 2 CG-TC SECCM imaging of transport with bulk n-WSe_2. (a) Optical transmission image of an exfoliated n-WSe_2 flake with a thickness of 25 nm. The region within this flake investigated *via* SECCM is indicated. (b) Photocurrent images at different potentials obtained in the vicinity of a focused 633 nm laser (1.12 μW). (c) Image of onset potentials (E_{on}), calculated as the potential necessary to reach a current of 100 pA. (d) Voltammograms obtained at different points along the dashed line in (b). The sweep rate was 0.20 V s^{-1}. All SECCM data was obtained using a ~600 nm diameter probe filled with 0.1 M NaI, 0.01 M I_2.

exhibiting a peaked profile that extends only a few μm from the excitation centroid. At more anodic potentials, the photocurrent profile significantly widens, eventually adopting a "top-hat" profile with a width of *ca.* 15 μm. A photocurrent movie is provided in the ESI† which provides a continuous visualization of this process (similar movies are also provided for Fig. 3 and 4).

As described in our previous report, the shape of this profile can be attributed to limitations on the mass transfer of redox species to the active interface in the SECCM geometry.[38] This mass-transfer limited current is:

$$i_{mt} \approx \frac{2\pi n q_e D_r C_r^* r_p (1 - \cos\theta_p)}{\tan\theta_p}$$

Here, n is the number of transferred electrons, q_e is the electronic charge, D_r is the diffusion coefficient of the redox active species, C_r^* is its bulk concentration, r_p is the pipet radius, and θ_p is the half-angle of the pipet. Using $n = 2/3$, $D = 2 \times 10^{-5}$ $cm^2\ s^{-1}$,[41] $C^* = 100$ mM, $r_p = 250$ nm, and $\theta_p = 10^\circ$ yields a value of ~2.4 nA, in good agreement with the plateaus in the observed profiles.

The widths of these profiles can be used to estimate the diffusion lengths of carriers in the material *via* comparison to finite element simulations which model carrier generation, recombination, and transport. The 15 μm widths observed here correspond to lateral carrier diffusion lengths of ~2.1 μm (see ESI† for details).

Fig. 2c presents these results in terms of onset potentials, defined as the potential necessary to reach an anodic photocurrent of 100 pA. Approaching the excitation centroid, the potential required to reach this threshold lowers at a rate of *ca.* 30 mV μm^{-1}. This reflects the larger potentials needed to concentrate holes at the electrochemical interface and drive the oxidation of iodide to an appreciable degree. Example voltammograms provided in Fig. 2d show the evolution of the photocurrent response starting at a distance far removed from the excitation source ($x = 3$ μm) and ending directly over the excitation centroid ($x = 17$ μm). Lower currents are observed far away from the excitation, attributable to limited carrier transport *via* diffusion. Increasingly larger currents are observed closer to the excitation source, eventually becoming limited by diffusion of redox species in the SECCM probe as discussed above. In all cases, a fairly simple sigmoidal response is obtained, though oscillatory behaviour can be observed at high current densities within the plateau region, which is the result of I_2 formation on the WSe_2 surface.[42]

Transport within WSe_2 bilayers

CG-TC SECCM was then applied to visualize carrier transport within few-layer WSe_2 structures. Samples were mechanically exfoliated as before, and photoluminescence (PL) imaging was employed to identify mono/bilayer structures based on the emergent PL properties of WSe_2 at this scale. Data acquired at a bilayer is displayed in Fig. 3. Optical transmission and PL images of the bilayer are provided in Fig. 3a. The dimensions of the bilayer region were roughly 10×90 μm, and the sample displayed significant PL across this entire region. The PL spectra (Fig. 3c) shows a broad (FWHM ≈ 100 meV) peak centered around 1.6 eV, attributable to an overlap of exciton emission and indirect band gap emission.[43,44]

Photocurrent images obtained in a continuous region of the bilayer are displayed in Fig. 3b. In the bilayer sample, the observed photocurrent profiles are

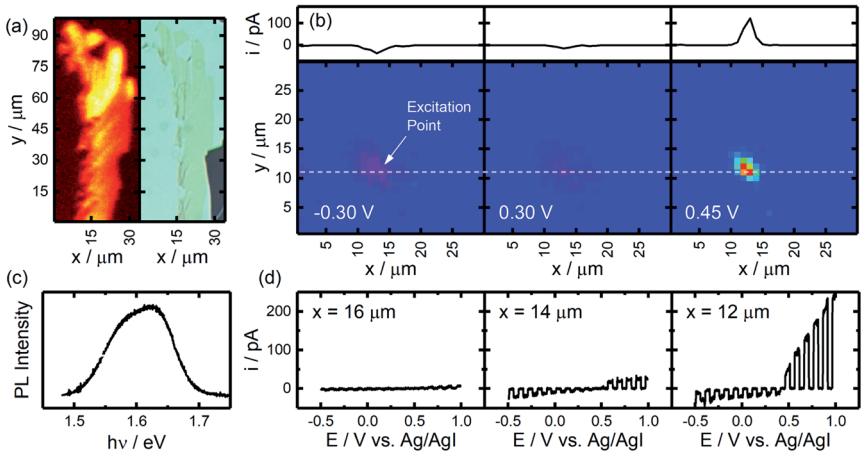

Fig. 3 CG-TC SECCM imaging of transport within a WSe_2 bilayer. (a) Optical transmission and photoluminescence (PL) images of an exfoliated WSe_2 bilayer. (b) Photocurrent images at different potentials obtained in the vicinity of a chopped (20 Hz), focused 633 nm laser (0.5 μW). (c) PL spectrum acquired from the layer. (d) Voltammograms obtained at different points along the white dashed line in (b). The sweep rate was 0.20 V s^{-1}. All SECCM data was obtained using a ~600 nm diameter probe filled with 0.1 M NaI, 0.01 M I_2.

much narrower than those observed in bulk samples, essentially overlapping with the laser profile (see Fig. S2 in the ESI†). This suggests the lateral diffusion of photogenerated excitons is profoundly limited compared to the bulk example. This is likely attributable to an increase in exciton recombination arising from a higher density of defects in the bilayer sample. The PL image provided in Fig. 3a supports this assertion, as significant intensity fluctuations are seen across the bilayer structure, reflecting the influence of nonradiative exciton recombination at defects.

Example voltammograms are provided in Fig. 3d. The bilayer exhibits a photoconductivity-type response, generating photocurrents at both cathodic and anodic potentials. The polarity of the photocurrents changes at a potential of ~0.5 V *vs.* Ag/AgI, which corresponds to the flat-band potential within the WSe_2 bilayer. The observed photocurrents, which reach maximum values of *ca.* 200 pA, are also much lower than one would expect. At 633 nm, a bilayer can be estimated to absorb roughly 12% of incident radiation,[44] yet these photocurrents reflect an incident photon to electron conversion efficiency of only 0.07%. This low efficiency, as well as the significant potential dependence in the observed photocurrents, may be attributable to an additional transport mechanism which drives carriers away from the probe–TMD interface, arising from the formation of interlayer excitons (see below).

Transport of excitons generated within monolayered WSe_2

Results from experiments of a more complex structure incorporating a WSe_2 monolayer are depicted in Fig. 4. An optical reflection image of the exfoliated flake is given in Fig. 4a, which allows six distinct regions of varying thickness to be

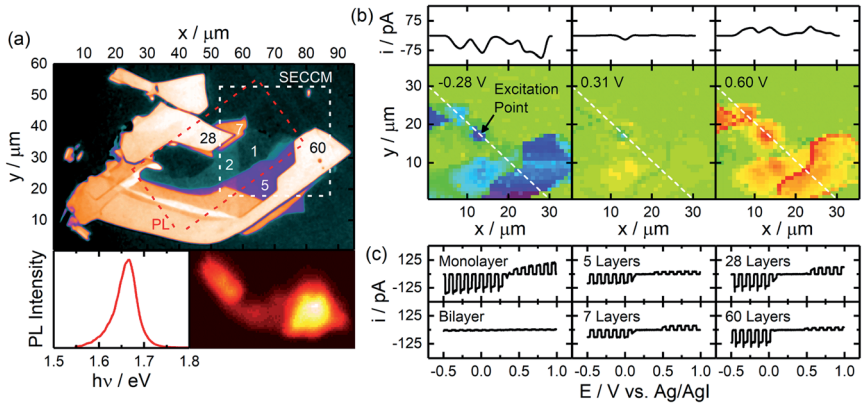

Fig. 4 CG-TC SECCM imaging of transport within a complex WSe_2 structure. (a) False color optical reflection and photoluminescence (PL) images of an exfoliated WSe_2 structure. The number of WSe_2 layers in different regions established *via* AFM measurements are indicated. A PL spectrum acquired from the monolayer is given below. (b) Photocurrent images at different potentials obtained in the vicinity of a chopped (20 Hz), focused 633 nm laser (0.4 μW). (c) Voltammograms obtained at different points along the white dashed line in (b). The sweep rate was 2.0 V s^{-1}. All SECCM data was obtained using a ~600 nm diameter probe filled with 0.1 M NaI, 0.01 M I_2.

easily distinguished. The thickness of each region was confirmed *via* AFM, and layer numbers are indicated in the provided image. A trapezoidal monolayer region was identified and confirmed *via* PL spectroscopy, exhibiting the sharp, intense emission typical of monolayered WSe_2.[44]

CG-TC SECCM images obtained for this sample are given in Fig. 4b. The sample was illuminated within the monolayer region, and SECCM measurements were obtained within a 35 μm × 35 μm region surrounding the excitation centroid, encompassing the area indicated in Fig. 4a. Significant cathodic (blue) and anodic (red) photocurrents were observed within the monolayer region surrounding the excitation centroid. However, in stark contrast to the bilayer sample, photocurrents can be observed throughout the entire sample area imaged *via* SECCM. Photocurrents observed in thicker regions of the sample are comparable in magnitude to those in the immediate vicinity of the excitation, while thinner regions display diminished photocurrents. Some spatial heterogeneity within these regions could be observed, likely due to the proximity of step-edge defects between adjacent regions. Due to the large carrier diffusion lengths observed here, it is unlikely that variations in sample–substrate contact could explain these effects. At anodic potentials, enhanced currents can be visualized at step-edge defects between adjacent regions, attributable to enhanced iodide oxidation kinetics. A notable feature in these images is the almost complete absence of observable photocurrents in the bilayer region (left-middle).

Example voltammograms obtained within each of the distinct thickness regimes are given in Fig. 4c. The general behaviour is similar to that of the bilayer, exhibiting photocurrents at both cathodic and anodic potentials. However, a significant splitting between the cathodic and anodic branches is observed which increases with increasing layer thickness. These trends are summarized in

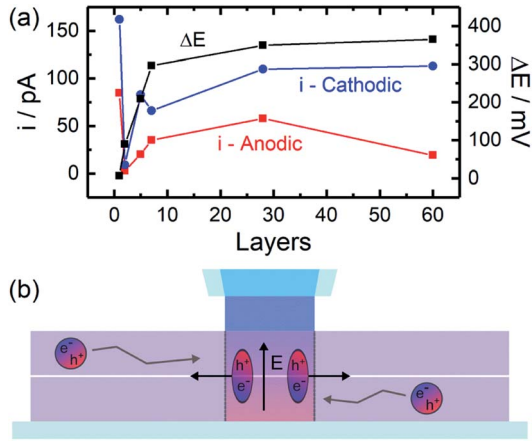

Fig. 5 (a) Relationships between layer thickness, photocurrents, and potential splitting between cathodic and anodic photocurrent branches (ΔE). (b) Illustration of the proposed mechanism responsible for negligible photocurrents in WSe_2 bilayers observed *via* SECCM.

Fig. 5a. This splitting can be attributed to the establishment of a field necessary to drive the transport of carriers vertically within the WSe_2 structure, requiring greater potentials within thicker regions.

Anomalous transport within monolayered WSe_2

Two features of the data presented in Fig. 4 warrant further discussion. First, the CG-TC experiments reveal that photogenerated excitons in monolayered WSe_2 can effectively drive photoelectrochemical reactions across distances in excess of 20 μm, much farther than the diffusion lengths estimated in previous studies on samples supported on inert substrates using optical techniques (<1 μm).[21,22] The ITO-supported WSe_2 monolayer studied here displayed PL lifetimes of *ca.* 1 ns (see Fig. S3 in the ESI†), which are roughly an order of magnitude greater than commonly reported values.[43,45] This discrepancy suggests long-lived charge transfer states exist which increase the effective lifetime and/or diffusion of photogenerated excitons. While more studies are needed to elucidate the origin of these effects, the data presented here nevertheless shows studies on idealized, encapsulated model systems may not meaningfully reflect how these materials will perform in practical devices.

The second notable feature is the significantly lower photocurrents observed at WSe_2 bilayers in the CG-TC SECCM experiments. This may be attributable to the field-driven formation of interlayer excitons in a bilayer structure, an effect which has been demonstrated to occur previously in homobilayers.[45] This idea is depicted schematically in Fig. 5b. In a bilayer structure, photogenerated excitons which diffuse to the pipet interface may be converted into interlayer excitons due to the large ($>10^6$ V cm^{-1}) fields present. These interlayer species would then be repelled from one another due to electrostatic interactions, which has been shown to enhance transport in bilayer systems as well as heterostructures.[6,24,45] In the present experiments, similar effects would cause excitons within bilayers to be

repelled from the probe–sample interface, significantly lowering the currents observable within these regions.

Conclusions

In this report, carrier generation-tip collection scanning electrochemical microscopy (CG-TC SECCM) was applied to visualize carrier transport in WSe_2 structures with thicknesses spanning the bulk (>10 nm) and monolayer levels. Using CG-TC SECCM, photogenerated carriers in bulk n-WSe_2 were found to exhibit diffusion lengths of *ca.* 2 μm. In the bilayer sample investigated, very short diffusion lengths were observed, attributable to a high density of defects present in the bilayer structure. The most striking results were obtained for the investigated monolayer sample, where photogenerated carriers were found to drive reactions over distances in excess of 20 μm. These studies provide powerful new insight into the transport of photogenerated carriers in complex 2DSC structures, and further demonstrate the power of electrochemical approaches for studying transport in these systems.

Author contributions

CLT and CMH designed the experiments. CLT acquired all the data. CLT and CMH analysed the data and wrote the manuscript.

Conflicts of interest

The authors have no conflicts to declare.

Acknowledgements

The authors acknowledge generous support for this work from the National Science Foundation (CHE-2045593), the University of Wyoming, and the Wyoming NASA Space Grant Consortium (NASA Grant #NNX15AI08H). The authors would also like to thank Dr Bruce Parkinson for his generous donation of WSe_2 crystals.

References

1 K. S. Novoselov, D. Jiang, F. Schedin, T. J. Booth, V. V. Khotkevich, S. V. Morozov and A. K. Geim, *Proc. Natl. Acad. Sci. U. S. A.*, 2005, **102**, 10451–10453.
2 Z. Zeng, Z. Yin, X. Huang, H. Li, Q. He, G. Lu, F. Boey and H. Zhang, *Angew. Chem.*, 2011, **123**, 11289–11293.
3 K. F. Mak, C. Lee, J. Hone, J. Shan and T. F. Heinz, *Phys. Rev. Lett.*, 2010, **105**, 2–5.
4 W. Zhao, Z. Ghorannevis, L. Chu, M. Toh, C. Kloc, P.-H. Tan and G. Eda, *ACS Nano*, 2013, **7**, 791–797.
5 A. Splendiani, L. Sun, Y. Zhang, T. Li, J. Kim, C. Y. Chim, G. Galli and F. Wang, *Nano Lett.*, 2010, **10**, 1271–1275.

6 D. Unuchek, A. Ciarrocchi, A. Avsar, Z. Sun, K. Watanabe, T. Taniguchi and A. Kis, *Nat. Nanotechnol.*, 2019, **14**, 1104–1109.
7 K. Behnia, *Nat. Nanotechnol.*, 2012, **7**, 488–489.
8 D. Jariwala, A. R. Davoyan, J. Wong and H. A. Atwater, *ACS Photonics*, 2017, **4**, 2962–2970.
9 K. Sivula and R. van de Krol, *Nat. Rev. Mater.*, 2016, **1**, 15010.
10 T. Mueller and E. Malic, *npj 2D Mater. Appl.*, 2018, **2**, 1–12.
11 D. Akinwande, N. Petrone and J. Hone, *Nat. Commun.*, 2014, **5**, 5678.
12 D. Jariwala, V. K. Sangwan, L. J. Lauhon, T. J. Marks and M. C. Hersam, *ACS Nano*, 2014, **8**, 1102–1120.
13 H. Hosono, *Thin Solid Films*, 2007, **515**, 6000–6014.
14 L. Wang, L. Huang, W. C. Tan, X. Feng, L. Chen, X. Huang and K.-W. Ang, *Small Methods*, 2018, **2**, 1700294.
15 G. Wang, A. Chernikov, M. M. Glazov, T. F. Heinz, X. Marie, T. Amand and B. Urbaszek, *Rev. Mod. Phys.*, 2018, **90**, 21001.
16 A. Steinhoff, M. Rösner, F. Jahnke, T. O. Wehling and C. Gies, *Nano Lett.*, 2014, **14**, 3743–3748.
17 M. Koperski, M. R. Molas, A. Arora, K. Nogajewski, A. O. Slobodeniuk, C. Faugeras and M. Potemski, *Nanophotonics*, 2017, **6**, 1289–1308.
18 K. He, N. Kumar, L. Zhao, Z. Wang, K. F. Mak, H. Zhao and J. Shan, *Phys. Rev. Lett.*, 2014, **113**, 1–5.
19 T. Cheiwchanchamnangij and W. R. L. Lambrecht, *Phys. Rev. B: Condens. Matter Mater. Phys.*, 2012, **85**, 205302.
20 A. Ramasubramaniam, *Phys. Rev. B: Condens. Matter Mater. Phys.*, 2012, **86**, 115409.
21 D. F. Cordovilla Leon, Z. Li, S. W. Jang, C.-H. Cheng and P. B. Deotare, *Appl. Phys. Lett.*, 2018, **113**, 252101.
22 F. Cadiz, C. Robert, E. Courtade, M. Manca, L. Martinelli, T. Taniguchi, K. Watanabe, T. Amand, A. C. H. Rowe, D. Paget, B. Urbaszek and X. Marie, *Appl. Phys. Lett.*, 2018, **112**, 152106.
23 L. Yuan, T. Wang, T. Zhu, M. Zhou and L. Huang, *J. Phys. Chem. Lett.*, 2017, **8**, 3371–3379.
24 L. Yuan, B. Zheng, J. Kunstmann, T. Brumme, A. B. Kuc, C. Ma, S. Deng, D. Blach, A. Pan and L. Huang, *Nat. Mater.*, 2020, **19**, 617–623.
25 Q. Cui, F. Ceballos, N. Kumar and H. Zhao, *ACS Nano*, 2014, **8**, 2970–2976.
26 J. T. Mefford, A. R. Akbashev, M. Kang, C. L. Bentley, W. E. Gent, H. D. Deng, D. H. Alsem, Y.-S. Yu, N. J. Salmon, D. A. Shapiro, P. R. Unwin and W. C. Chueh, *Nature*, 2021, **593**, 67–73.
27 R. G. Mariano, M. Kang, O. J. Wahab, I. J. McPherson, J. A. Rabinowitz, P. R. Unwin and M. W. Kanan, *Nat. Mater.*, 2021, **20**, 1000–1006.
28 J. W. Hill, Z. Fu, J. Tian and C. M. Hill, *J. Phys. Chem. C*, 2020, **124**, 17141–17149.
29 L. E. Strange, J. Yadav, S. Garg, P. S. Shinde, J. W. Hill, C. M. Hill, P. Kung and S. Pan, *J. Phys. Chem. Lett.*, 2020, **11**, 3488–3494.
30 O. J. Wahab, M. Kang and P. R. Unwin, *Curr. Opin. Electrochem.*, 2020, **22**, 120–128.
31 E. Daviddi, Z. Chen, B. Beam Massani, J. Lee, C. L. Bentley, P. R. Unwin and E. L. Ratcliff, *ACS Nano*, 2019, **13**, 13271–13284.

32 C. L. Bentley, J. Edmondson, G. N. Meloni, D. Perry, V. Shkirskiy and P. R. Unwin, *Anal. Chem.*, 2019, **91**, 84–108.
33 C. L. Bentley, M. Kang and P. R. Unwin, *J. Am. Chem. Soc.*, 2017, **139**, 16813–16821.
34 B. Tao, P. R. Unwin and C. L. Bentley, *J. Phys. Chem. C*, 2020, **124**, 789–798.
35 M. Kang, D. Perry, C. L. Bentley, G. West, A. Page and P. R. Unwin, *ACS Nano*, 2017, **11**, 9525–9535.
36 M. E. Snowden, A. G. Güell, S. C. S. Lai, K. McKelvey, N. Ebejer, M. A. O'Connell, A. W. Colburn and P. R. Unwin, *Anal. Chem.*, 2012, **84**, 2483–2491.
37 J. W. Hill and C. M. Hill, *Nano Lett.*, 2019, **19**, 5710–5716.
38 J. W. Hill and C. M. Hill, *Chem. Sci.*, 2021, **12**, 5102–5112.
39 H. J. Lewerenz, S. D. Ferris, C. J. Doherty and H. J. Leamy, *J. Electrochem. Soc.*, 1982, **129**, 418.
40 A. Laturia, M. L. Van de Put and W. G. Vandenberghe, *npj 2D Mater. Appl.*, 2018, **2**, 6.
41 *CRC Handbook of Chemistry and Physics*, ed. D. R. Lide, CRC Press, 89th edn, 2008.
42 H. Tributsch, *J. Electrochem. Soc.*, 1978, **125**, 1086–1093.
43 T. Yan, X. Qiao, X. Liu, P. Tan and X. Zhang, *Appl. Phys. Lett.*, 2014, **105**, 101901.
44 W. Zhao, Z. Ghorannevis, L. Chu, M. Toh, C. Kloc, P.-H. Tan and G. Eda, *ACS Nano*, 2013, **7**, 791–797.
45 Z. Wang, Y.-H. Chiu, K. Honz, K. F. Mak and J. Shan, *Nano Lett.*, 2018, **18**, 137–143.

